Mechanisms of Porphyroblast Crystallization: Results from High-Resolution Computed X-ray Tomography

William D. Carlson* and Cambria Denison

Quantitative three-dimensional analysis of rock textures is now possible with the use of high-resolution computed x-ray tomography. When applied to metamorphic rocks, this technique provides data on the sizes and positions of minerals that allow mechanisms of porphyroblast crystallization to be identified. Statistical analysis of the sizes and spatial disposition of thousands of garnet crystals in three regionally metamorphosed rocks with diverse mineralogies, in conjunction with simple numerical models for crystallization, reveals in all cases the dominance of crystallization mechanisms whose kinetics are governed by rates of intergranular diffusion of nutrients.

Metamorphic minerals grow in nature at rates that are many orders of magnitude too slow to permit kinetically equivalent replication of the mineralogic reactions in the laboratory (1), so mechanisms of metamorphic reactions must often be inferred from rock textures. Conceptual links have been established between reaction mechanisms and key textural features such as the size and spatial disposition of porphyroblasts (2–4); this connection demonstrates that knowledge of the mechanisms of porphyroblast crystallization may lead to quantification of the rates of essential metamorphic processes. Toward this end, theories of metamorphic crystallization have focused on the relative significance of growth mechanisms governed by rates of interface reaction, intergranular diffusion, and heat flow (5).

Progress toward identifying the actual crystallization mechanisms that dominate in nature, however, has so far been limited by difficulties in securing suitable textural data. Conventional analysis of rocks in thin section (2) has crippling drawbacks, including limitations of small scale and the inherent corruption of the data that results from examining isolated two-dimensional sections through a three-dimensional system. Occurrences in which crystals are serendipitously localized in nearly coplanar arrays (3, 4) are too rare to be of general utility. Painstaking efforts in which three-dimensional data are obtained from serial sectioning or crystal-by-crystal dissection (6) produce data sets in which the number of crystals that can be examined without unconscionably arduous effort (rarely more than a few score) may be too small to yield statistical significance. In this report we describe the advent of high-resolution computed x-ray tomography as a tool for three-dimensional quantitative textural analysis

of rocks and use this method to obtain data on the sizes and spatial disposition of garnet crystals in regionally metamorphosed rocks from three localities; with these data, we assess mechanisms governing porphyroblast crystallization.

The industrial x-ray tomographic analyzer we used is conceptually similar to instruments used for medical diagnosis (7). In contrast to typical medical CAT-scanners, however, it is capable of significantly higher x-ray intensity and markedly higher spatial resolution, on the order of tenths of milli-

meters compared to millimeters. Each tomographic image (Fig. 1, A to C) represents density variations in a planar slab of the specimen (8); the thickness of each such slab is determined by the final x-ray apertures (0.25 or 0.50 mm in this work). The images in a stack of contiguous slabs constitute a three-dimensional map of density in the sample (Fig. 1D) from which one can extract the sizes, locations, densities, and shapes of individual crystals that have dimensions larger than the spatial resolution of the scans. In addition, one obtains the average density of finer grained regions, such as the matrix surrounding a porphyroblast.

We examined three garnetiferous rocks that display contrasts in bulk composition and mineralogy, in the timing of garnet growth relative to deformation, and in the degree of homogeneity of the matrix from which the porphyroblasts grew. Sample PM (Fig. 1A) is a feldspathic quartzite with abundant almandine-rich garnet and minor biotite from the Picuris Mountains of north-central New Mexico (3, 4). It was selected as an example of post-kinematic crystallization from a nearly homogeneous semipelitic precursor. Sample WR (Fig. 1B) is a garnet amphibolite from the Whitt Ranch in the Llano Uplift of central Texas, in which almandine and pseudomorphs of oligoclase, augite, and hornblende after
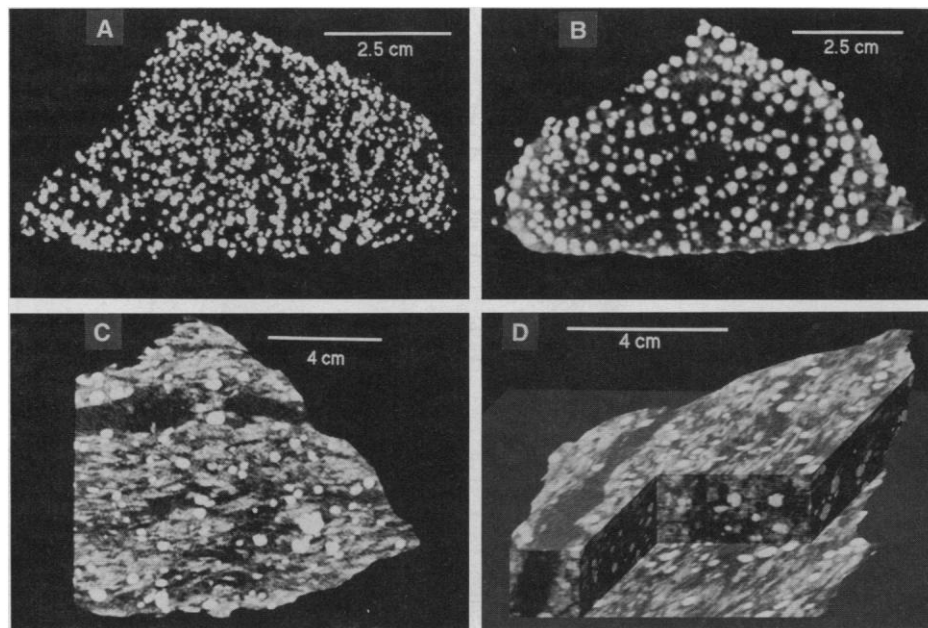
Fig. 1. X-ray tomographic images of garnetiferous metamorphic rocks. Brightness in images correlates with mineral density; more dense minerals appear in lighter shades of gray. (**A**) Garnetiferous quartzite, sample PM; single slice. Garnets are white; quartzofeldspathic matrix is black. (**B**) Garnet amphibolite, sample WR; single slice. Garnets are white; fine-grained matrix of pyroxene, amphibole, and plagioclase is black. (**C**) Pelitic schist, sample MD; single slice. Garnets are light gray to white ovals; kyanite porphyroblasts appear as medium-gray laths. Medium-gray to dark gray regions are rich in fine-grained biotite and kyanite; dark gray to black regions are rich in fine-grained quartz, feldspar, and muscovite. A discontinuous quartz vein about 1 cm wide appears as a black band at top-center. (**D**) Pelitic schist, sample MD; perspective view of three-dimensional density map. Single slice at bottom of stack serves to locate cutaway block in interior of specimen.

Department of Geological Sciences, University of Texas at Austin, Austin, TX 78712.

*To whom correspondence should be addressed.

omphacite form an equigranular mosaic lacking any penetrative fabric (9). It was selected as an example of garnet crystallization from a nearly homogeneous mafic precursor in which deformation during garnet growth was negligible. Sample MD (Fig. 1, C and D) is an almandine-kyanite mica schist from the Mica Dam locality in British Columbia (10). It was selected as an example of synkinematic garnet crystallization from a pelitic precursor that had a strong penetrative fabric and distinct compositional inhomogeneities (11).

As shown in Fig. 1, detailed textural information can be obtained from the high-resolution computed tomography (CT) scans. From such imagery, it was possible to locate the center of each garnet crystal to within ±0.25 mm in each dimensional coordinate and to assign to each (as an average radius) the radius of a sphere whose volume is equal to the measured volume of the crystal (12). Table 1 lists the number of porphyroblasts and total volume of rock analyzed in each sample. Without comprehensive three-dimensional data of this sort, and without measurements this numerous, one cannot extract reliable information on crystallization processes from textures that reflect substantial stochastic variations.

Spatial dispositions of porphyroblasts convey information about crystallization processes because atomic-scale mechanisms governed by the rates of intergranular diffusion produce (from a uniformly distributed set of potential sites for nucleation) a partially ordered spatial arrangement of crystals, whereas other possibilities, such as interface-controlled mechanisms and heat flow–controlled mechanisms, produce random arrangements (2, 6). Diffusion-controlled kinetics generate a tendency toward spatial ordering because each growing porphyroblast becomes surrounded by a nutrient-depleted zone in which a lower chemical affinity for reaction suppresses subsequent nucleation (3, 4). Within inhomogeneous precursors, however, localization of potential nucleation sites in compositionally more favorable regions of the rock may produce clusters of crystals, within which diffusional ordering may still occur.

Conventional interpretations of spatial dispositions thus pivot upon the extent to which crystal centers depart from a random arrangement (2, 3, 13). We applied four tests of spatial randomness to the locations of crystal centers in samples PM, WR, and MD (Table 1) (14). The quadrat χ^2 statistic compares the frequency distribution of the number of crystal centers falling inside a randomly placed quadrat with a Poisson distribution; the values of this statistic demonstrate that the crystal centers depart significantly from a random array in all samples, but this test yields no information on

the character of the nonrandomness. The nearest-neighbor index compares the mean center-to-center distance for nearest-neighbor crystals with that distance for a random array of centers of the same spatial density; the values of this statistic imply that crystal centers are spatially ordered in all samples. The random-point index compares the mean distance to the nearest crystal center from a randomly placed point with that distance in a random array of centers; the values of this statistic indicate that crystals are significantly clustered in samples WR and MD, but reflect no significant departure from randomness for sample PM. The impingement index compares the amount of interpenetration of adjacent crystals to the amount characterizing a set of randomly disposed crystals; the values of this statistic indicate that the spatial dispositions in all three samples are significantly ordered relative to a random distribution.

The detection of both clustering and ordering by different statistical tests suggests that despite some localization of nuclei into regions of favorable composition, crystals within those regions are spatially ordered. This inference is supported by numerical simulations of crystallization from a homogeneous matrix (15) in which nuclei are localized into one or more clusters, but ordered within those clusters by diffusional suppression of nucleation close to preexisting crystals. The behavior of the statistics in these simulations of diffusion-controlled growth of clustered crystals mirrors that seen for the natural samples shown in Table 1: the simulations demonstrate that the random-point index is particularly sensitive to clustering effects, that the impingement index retains strong sensitivity to ordering even in clustered arrangements, and that

the nearest-neighbor index is influenced by both effects in roughly equal measure.

The operation of a diffusion-controlled nucleation-and-growth mechanism is further confirmed in these samples by a relation between crystal size and the degree of isolation of each crystal. If the crystallization mechanism is governed either by the rate of interface reaction or by the rate of heat flow, the size of a crystal and its degree of isolation should be unrelated, because nutrients remain uniformly available throughout the matrix during the entire crystallization process. In a diffusion-controlled nucleation-and-growth process, however, adjacent porphyroblasts compete with one another for nutrients during growth. Thus, diffusional kinetic controls should produce a texture in which the size of a crystal is related to the size of the domain from which it would extract nutrients in a competitive diffusion-controlled process. If nutrients are initially distributed homogeneously throughout the rock at scales larger than the precursor grain size, the relation should be perfectly linear, but inhomogeneities in the initial distribution of nutrients will generate scatter. Clustering of nuclei, however, will not degrade the linear relation. The relative insensitivity of this test to local variations in nucleation-site density makes it our most useful tool for extracting information on crystallization mechanisms in inhomogeneous samples.

In earlier work, Carlson (4) introduced several methods for estimation of sizes of diffusional domains, focusing on the calculation of Voronoi polyhedra and modified Voronoi regions. Voronoi polyhedra enclose the set of points around a crystal that are closer to that crystal than to any other; modified Voronoi regions include all points

Table 1. Spatial dispositions of garnet porphyroblasts from x-ray tomography.

	Sample PM	Sample WR	Sample MD
CT slice thickness (mm)	0.25	0.25	0.50
Number of slices	79	80	60
Number of porphyroblasts	6584	4755	1268
Volume of rock analyzed (cm³)	28.6	56.4	171.9
Quadrat χ^2 statistic ($\geq$12.6)*	22.8	24.6	19.3
Nearest-neighbor index	1.23	1.19	1.10
t-test for ordering ($\geq$1.65)*	5.57	4.59	1.93
Random-point index ($\geq$1.05)*	1.02	1.10	1.22
Impingement index ($\leq$0.98)*	0.84	0.88	0.97
Test of size-isolation relation			
Number of data pairs†	4828	3076	568
Regression slope ± SE	0.315 ± 0.009	0.314 ± 0.010	0.028 ± 0.011
Probability‡	<10⁻⁶	<10⁻⁶	0.011
Regression intercept ± SE	0.00043 ± 0.00004	−0.0007 ± 0.0001	0.008 ± 0.002
Coefficient of linear correlation	0.43	0.50	0.11
Probability§	<10⁻⁶	<10⁻⁶	0.009

*Numbers in parentheses are critical values at the 95% confidence level. †Excludes all domains that intersect the convex hull enclosing the set of crystal centers. ‡Probability that slope of regression line is not different from zero. §Probability of obtaining or exceeding the observed correlation coefficient in a random sampling of an uncorrelated parent population.
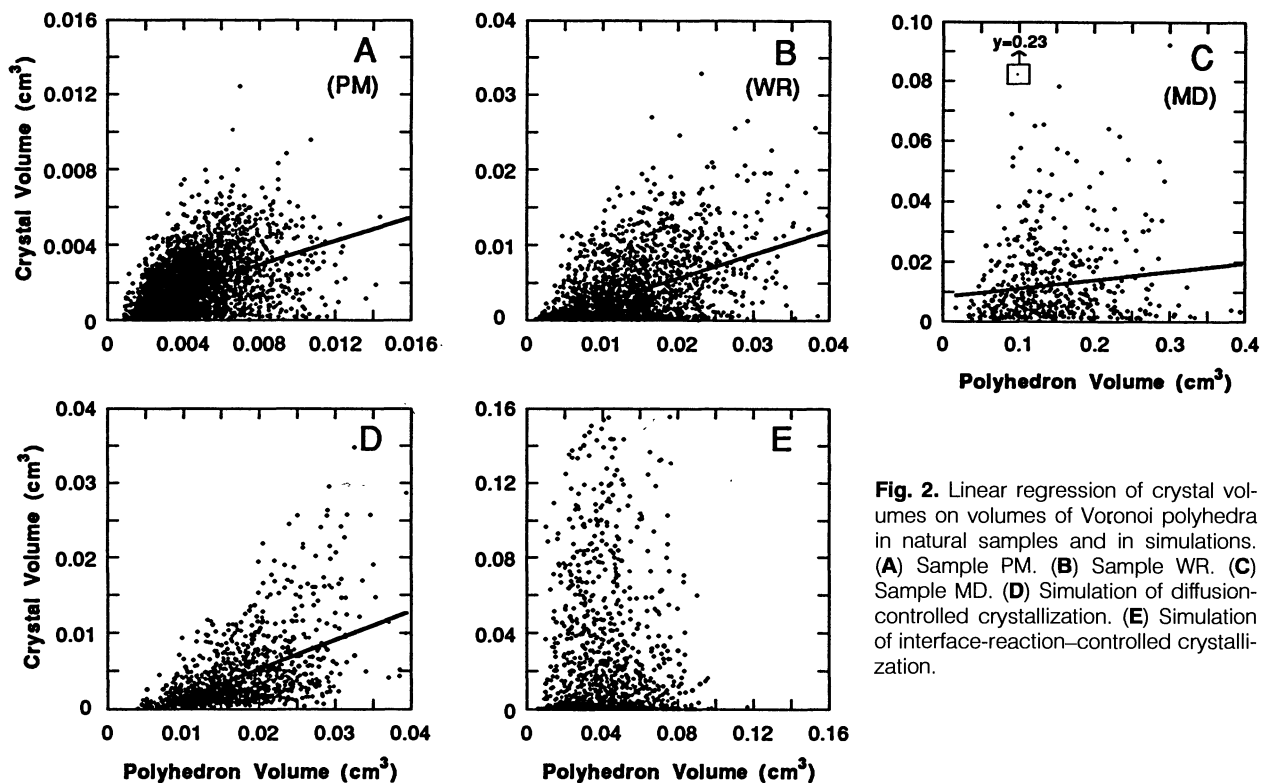
Fig. 2. Linear regression of crystal volumes on volumes of Voronoi polyhedra in natural samples and in simulations. (**A**) Sample PM. (**B**) Sample WR. (**C**) Sample MD. (**D**) Simulation of diffusion-controlled crystallization. (**E**) Simulation of interface-reaction–controlled crystallization.

in the rock belonging to the diffusional domain of a crystal, as calculated under the simplifying assumption that relative times of nucleation can be derived from relative crystal sizes. Because the estimation of modified Voronoi regions incorporates crystal size as a determinant of relative nucleation time, this calculation can generate a spurious positive relation between the volume of the modified Voronoi region and the crystal volume. We therefore prefer the use of Voronoi polyhedra as approximations to the diffusional domains when seeking to identify crystallization mechanisms.

As shown in Fig. 2, A to C, a linear relation between crystal volume and Voronoi polyhedral volume is present in all three samples, although it is expressed to varying degrees in each. The regression lines in all cases have slopes significantly different from zero and pass nearly through the origin, and the coefficients of linear correlation reflect negligible probabilities that the data sample an uncorrelated parent population (Table 1). These linear relations emerge from the noisy data principally because of the large numbers of porphyroblasts for which the CT imagery provides information. Scatter in the data reflects both inhomogeneity in the initial distribution of nutrients (16) and the fact that Voronoi polyhedra are only coarse approximations to the actual diffusion domains (17). The scatter resulting from the latter factor has been assessed in a series of numerical simulations of diffusion-controlled

crystallization from a homogeneous precursor (15). In these simulations, crystal volumes are exactly proportional to volumes of diffusional domains, but the crystal volumes scatter when plotted against the volumes of Voronoi polyhedra. For a typical simulation (Fig. 2D), the statistics describing the relation between the variables (slope = 0.383 ± 0.017; intercept = −0.0025 ± 0.0003; correlation coefficient = 0.53) are commensurate with those that characterize the two nearly homogeneous natural samples PM and WR. Despite scatter about the best-fit line, the test for a linear relation between crystal volume and Voronoi polyhedral volume remains a sensitive indicator of mechanism: Fig. 2E illustrates the absence of a significant linear relation in a typical simulation of interface reaction–controlled crystallization.

We conclude that in each of these samples, representing three common bulk compositions over a range of typical regional-metamorphic environments, garnet crystallization took place by mechanisms whose kinetics are governed predominantly by rates of intergranular diffusion. This result for sample PM corroborates earlier work on samples from this locality for which garnet zoning patterns provided compelling additional evidence for such mechanisms (3). The unanticipated similarity of results from the other two samples implies that these crystallization mechanisms may operate more generally during the formation of garnet in regional-metamorphic rocks.

With high-resolution x-ray tomography as a new tool for quantitative textural analysis, it is now opportune to ask and feasible to determine whether such mechanisms govern nucleation-and-growth kinetics for other crystals in other geologic environments.

REFERENCES AND NOTES

1. J. N. Christensen, J. L. Rosenfeld, D. J. DePaolo, Science 244, 1465 (1989); D. Vance and R. K. O'Nions, Earth Planet. Sci. Lett. 97, 227 (1990); K. W. Burton and R. K. O'Nions, ibid. 107, 649 (1991).
2. R. Kretz, Lithos 2, 39 (1969).
3. W. D. Carlson, Contrib. Mineral. Petrol. 103, 1 (1989).
4. _____, Mineral. Mag. 55, 317 (1991).
5. G. W. Fisher, Geochim. Cosmochim. Acta 42, 1035 (1978).
6. R. Kretz, J. Geol. 74, 147 (1966).
7. G. N. Hounsfield, Br. J. Radiol. 46, 1016 (1973).
8. Tomographic images were obtained commercially (Scientific Measurement Systems, Austin, TX) on an industrial tomographic scanner (SMS Model 101B+) with a tungsten x-ray source operating at 420 kV and 3 mA; a 0.315-cm brass filter was used on samples PM and MD to reduce beam-hardening artifacts. Exposure times were approximately 5 min per slice. Images were reconstructed with a filtered-backprojection algorithm.
9. W. D. Carlson and C. D. Johnson, Am. Mineral. 76, 756 (1991).
10. P. S. Simony, E. D. Ghent, D. Craw, W. Mitchell, D. B. Robbins, Geol. Soc. Am. Mem. 153, 445 (1980).
11. Only those crystals within the volume below the quartz vein in Fig. 1C were included in the quantitative analysis.
12. The resulting crystal size distributions are pseudo-normal with positive skewness, typical of size distributions for metamorphic porphyroblasts [(2, 3, 6); K. V. Cashman and J. M. Ferry, Contrib. Mineral. Petrol. 99, 401 (1988)]; such distributions

do not, however, uniquely determine crystallization mechanisms (3).
13. G. J. G. Upton and B. Fingleton, *Spatial Data Analysis by Example*, vol. 1, *Point Pattern and Quantitative Data* (Wiley, Chichester, UK, 1985).
14. For details of the implementation of these tests, consult (3), in which identical procedures were followed.
15. These simulations use the same simple model for crystallization described in (4) but explore a wider range of possible cluster geometries.
16. Because marked inhomogeneity in the distribution of aluminous minerals is evident in Fig. 1C, this factor probably accounts for the relatively large scatter for sample MD.
17. See (4) for discussion of the relation between Voronoi polyhedra and the actual diffusional domains.

Mount Pinatubo Aerosols, Chlorofluorocarbons, and Ozone Depletion

Guy Brasseur and Claire Granier

The injection into the stratosphere of large quantities of sulfur during the June 1991 eruption of Mount Pinatubo (Philippines) and the subsequent formation of sulfate aerosol particles have generated a number of perturbations in the atmosphere with potential effects on the Earth's climate. Changes in the solar and infrared radiation budget caused by the eruption should produce a cooling of the troposphere and a warming of the lower stratosphere. These changes could affect atmospheric circulation. In addition, heterogeneous chemical reactions on the surface of sulfate aerosol particles render the ozone molecules more vulnerable to atmospheric chlorine and hence to man-made chlorofluorocarbons.

After having been inactive for 635 years, Mount Pinatubo in the Philippines (15.1°N, 120.4°E) injected 15 to 30 MT of sulfur dioxide (SO_2) into the stratosphere in mid-June 1991 (1–3). In about a month the SO_2 was converted into sulfuric acid (H_2SO_4), which in the stratosphere condenses into small particles (called aerosols) (4). The aerosol load after this volcanic eruption was one or two orders of magnitude larger than that produced by biological and anthropogenic sources (5). These small droplets are expected to remain in the atmosphere for 1 to 3 years (6).

In 1982, another volcano, El Chichón, located in Mexico (17.3°N, 92.3°W) at approximately the same latitude as Mount Pinatubo, injected 7 to 20 MT of SO_2 into the stratosphere (7). Several perturbations resulting from this eruption were reported (8), including an increase in the temperature of the lower stratosphere (9), probably a slight cooling of the surface (10), and a reduction in the concentration of stratospheric ozone (O_3) (11). The observed O_3 depletion is believed to be associated with heterogeneous chemical reactions involving nitrogen and chlorine compounds on the surface of the aerosols. Similar processes on the surfaces of ice particles in polar stratospheric clouds have led to the formation of the O_3 hole over Antarctica. Vol-

National Center for Atmospheric Research, Post Office Box 3000, Boulder, CO 80307.

canoes also release chlorine compounds but, after the eruption of Mount Pinatubo, the input of chlorine to the stratosphere was probably small (12).

Although both eruptions share several common features (for example, SO_2-rich plumes) (13), there were several differences in the fate and impact of the clouds [different phases in the quasi-biennial oscillation (QBO) of winds in the atmosphere and different atmospheric concentrations of anthropogenic chlorine and bromine] (14).

The gas-phase destruction of O_3 by chlorine in the lower stratosphere is relatively inefficient because the reactive Cl and ClO radicals are rapidly converted into less reactive compounds such as HCl and $ClONO_2$ (15). Because $ClONO_2$ is formed by the reaction of ClO with NO_2, the oxides of nitrogen are sometimes referred to as the "immune system" of the lower stratosphere.

Laboratory investigations have shown that heterogeneous chemical processes on the surface of aerosol particles convert nitrogen oxides (NO_x represents NO, NO_2, NO_3, and N_2O_5) into nitric acid (HNO_3) and hence weaken the "immune system" against chlorine in the atmosphere. The reaction involved is

$$N_2O_5 \text{ (gas)} + H_2O \text{ (aerosols)} \rightarrow 2 \, HNO_3 \text{ (gas)} \qquad (1)$$
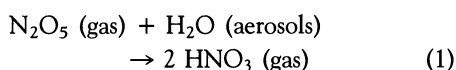
The probability that a collision of N_2O_5 with an aerosol particle results in the above reaction is of the order of 10 to 18% (16, 17). For background aerosol loads, the time required for this conversion is of the order of 1 day, so that, even during periods not perturbed by volcanic eruptions, reaction 1 is efficient and indirectly enhances the sensitivity of O_3 to chlorine in the lower stratosphere. The direct heterogeneous destruction of $ClONO_2$,

$$ClONO_2 \text{ (gas)} + H_2O \text{ (aerosols)} \rightarrow HNO_3 \text{ (gas)} + HOCl \text{ (gas)} \qquad (2)$$
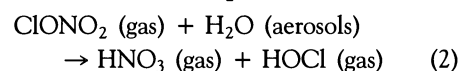
also contributes to the conversion of nitrogen oxides into HNO_3 but, in addition, converts $ClONO_2$ into HOCl. This latter molecule is rapidly photolyzed into reactive chlorine (Cl, ClO). The probability for reaction 2 to occur is significantly lower than that of reaction 1 and is further dependent on the chemical composition (for example, the H_2SO_4 percentage by weight) of the aerosol (18). This reaction, however, becomes efficient in very cold air masses (for example, at high latitudes in winter and spring).

After large volcanic eruptions, the surface area available for these heterogeneous reactions is increased by a factor of 10 to 100 (11), and substantial perturbations could occur. The concentration of nitrogen oxides is expected to be reduced while the concentrations of HNO_3 and ClO should be enhanced (19). At the same time, the concentration of hydroxyl (OH) and hydroperoxyl (HO_2) radicals should increase. Thus, after a large volcanic eruption, the atmosphere shifts from a situation in which O_3 is primarily controlled by nitrogen oxides to one in which the O_3 loss becomes largely controlled by chlorine compounds and HO_x radicals.

In order to assess the impact of the Mount Pinatubo eruption on the O_3 layer, we used a two-dimensional (latitude-altitude) model describing chemical, radiative, and dynamical processes in the middle atmosphere (20). The model extends from pole to pole and from the surface to an altitude of 85 km with a resolution of 5° in latitude and 1 km in altitude. Approximately 60 species and 115 chemical and photochemical reactions are included in the chemical scheme, including heterogeneous reactions 1 and 2. For reaction 1, the reaction probability is assumed to be 0.14 for all temperatures and aerosol compositions (16, 17), whereas for reaction 2 values of 3×10^{-2}, 1×10^{-2}, 5×10^{-3}, and 5×10^{4} are adopted for H_2SO_4 percentages by weight of 40, 50, 60, and 70%, respectively (18). A simplified parameterization of heterogeneous reactions in polar stratospheric clouds is also included.

Because the dispersion of the volcanic cloud and the microphysical transformation involved (nucleation, condensation, evap-